AerospaceEurope Conference2020
BORDEAUX, FRANCE | 25 - 28 FEBRUARY 2020
CEAS Council of European Aerospace Societies
HOSTED BY : 3AF Association Aéronautique et Astronautique de France

MINIATURE AIRWORTHY FIBER-OPTIC PRESSURE SENSOR FOR MEASURING STATIC PRESSURE AND ACOUSTICS

S. Kienitz [(1)], S. Kreft [(1)], M. Schmid[(1)], M. Staats[(2)], A. W. Koch[(3)]

[(1)] fos4X GmbH, Thalkirchnerstr. 210, 81371 Munich (Germany), Email: sascha.kienitz@fos4x.de
[(2)] Institute for Aerospace, Division Aerodynamics, Technische Universität Berlin (TUB), Marchstraße 12, 10587 Berlin (Germany), Email: marcel.staats@tub.de
[(3)] Institute for Measurement Systems and Sensor Technology (MST), Technical University of Munich (TUM), Theresienstrasse 90/N5, 80333 Munich (Germany)

KEYWORDS: fiber-optic, pressure sensing, acoustic measurement, unsteady pressure, Fabry-Pérot, aerodynamics

ABSTRACT:

Conventional electrical pressure sensors show a degradation of their performance in harsh environments, because of their low overload protection, drawn back membrane, susceptibility to electromagnetic influences and corrosion. Fiber-optic measurements overcome those challenges and promise to be a robust sensing solution for vigorous flight testing. We have developed a cylindrical passive fiber-optic Fabry-Pérot pressure sensor with a diameter of 2 mm, natural frequency above 250 kHz, linear transfer characteristic, burst pressure resistance above 30 times full-scale, and without conductive and corrosive materials. It is capable of measuring aerostatics, aerodynamics and aeroacoustic events down to 60dBSPL. In combination with an industrialized edge filter interrogator, the sensor performance was successfully evaluated in two wind tunnel tests. The results pave the way to perform in-flight measurements of time-resolved surface pressure measurement.

1. MOTIVATION

The main goal of today's civil aviation industry is to reduce CO_2 emissions, improve fuel consumption and moderate noise emissions of next-generation aircraft. In response, ultra-high bypass ratio engines (UHBR) are designed to contribute to a more ecologic and economical aircraft generation. The UHBR turbines demand a larger nacelle size. Therefore, the integration of those high and ultrahigh bypass ratio turbines on airframes are becoming more challenging as it is required to ensure enough clearance between the nacelle and the runway. In order to avoid more extensive and heavier landing gears, the UHBR turbines are not mounted directly under the wings but coupled closer to the front of the airfoil. In critical flight situations, the updated nacelle position is degrading the aerodynamics. Especially during the take-off and landing situations, when the aircraft is close to the critical stall condition, the risk of flow separation in the region of the wing pylon junction is more significant than with conventional airframe design. [2] Thereby, measurement of the local dynamic flow separation, complex vortex flows, and lift coefficients of real-sized aircraft are required to gain a better understanding of the prevalent aerodynamic and aeroacoustic effects. Conventional electrical pressure sensors show a degradation of their high performance in harsh environments during in-flight applications. Due to their low overload protection, a protected drawn back membrane, susceptibility to electromagnetic influences, and corrosion, they are limited in their lifetime for continuous flight application. Fiber-optic measurements promise to be a robust sensing solution for harsh flight tests because of the inherent advantages of fiber-optics [1]. Therefore, the scope of this research is the development of high dynamic pressure sensors in miniature size, which enable robust field tests of actual flight characteristics.

2. MEASUREMENT PRINCIPLE

A fundamental advantage of fiber-optic pressure sensors is the inherent immunity to parasitic electromagnetic fields as electromagnetic coupling. The influences of cable length and the triboelectric charging caused by colliding dust particles in the air will not affect the fiber-optic sensor reading. Besides, the temperature ranges of fiber-optic sensors are potentially wider compared to semiconductor-based pressure sensors. Because of the passive design, fiber-optic sensors are designed to operate explosion-proof, which allows the monitoring of flammable applications. The absence of corrosive materials allows greater load cycles, a longer lifetime, and, most importantly, excellent overload stability.

2.1. Fiber-optic Pressure Sensor

To exhibit the mentioned advantages of fiber-optics for pressure sensing applications, we developed a cylindrical passive fiber-optic Fabry–Pérot pressure sensor. The sensor features a diameter of 2 mm, a natural frequency above 250 kHz, linear transfer characteristic, burst pressure resistance above 30 times full-scale, and consists of no conductive and corrosive materials. It is capable of measuring aerostatic, aerodynamic and aeroacoustic events as a pressure sensor and as a microphone at the same time.

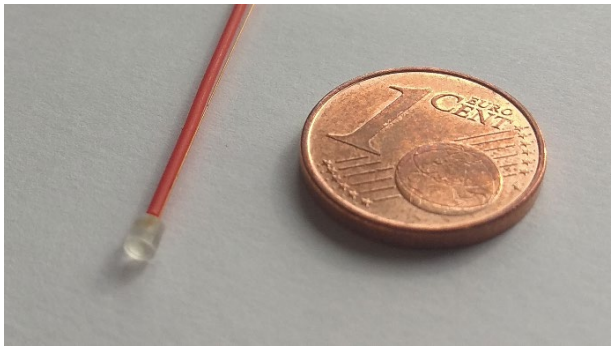

Figure 1. Miniature fiber-optic pressure sensor.

The durable cylindrical chip, micromachined in a selective laser etching process in pure glass, consists of a reflective diaphragm, resonance cavity, and single-mode fiber. Depending on the application, the sensor can be packaged as a sealed, differential device, or for absolute pressure sensing in a vacuum chamber. The fully exposed membrane at the front surface of the sensor enables pressure measurements of probes and test models in aerodynamic studies of complex unsteady flows without any spectral characterization.

The basic mechanical principle of this transducer is comparable with most electrical sensors. The mechanical deflection ΔL of a diaphragm depends on the applied pressure difference Δp, which, in turn, influences the optical properties of the sensors. By deriving Kirchhoff plate theory, the sensitivity of a three-dimensional circular diaphragm, as long as the geometry is uniform and the radius r is much larger than the thickness h, is described by equation 1.

$$\frac{\Delta L}{\Delta p} = \frac{r^4}{64\,K} \qquad (1)$$

In equation 1, the bending stiffness K is determined by material properties such as Young's modulus E and Poisson's ratio ν and is expressed in equation 2 [4].

$$K = \frac{Eh^3}{12\,(1-\nu^2)} \qquad (2)$$

The sensitivity of the membrane depends on the cube of the inverse of the thickness and the square of the radius. The fundamental challenge of the mechanical sensor design is to choose the thickness and the radius of the diaphragm to match the sensitivity and natural frequency of the transducer to the specific application. An additional constraint is the small sensor footprint, which enables capturing highly dynamic pressure gradients with multiple measuring points located close to each other. Moreover, for measuring aeroacoustics, another limitation is to maintain a constant frequency response up to 80% of the natural frequency, which is given in equation 3, considering ρ as material density.

$$f = \frac{10.2}{2\pi\, r^2}\sqrt{\frac{K}{h\rho}} \qquad (3)$$

By using finite element simulations, we realized more complex designs to simplify the manufacturing process, increase repeatability of transducer sensitivity, and reducing the effects of a tipping light path. The sensor is working as a Fabry-Pérot Interferometer, which is based on the superposition of optical waves. If a light source illuminates the sensor from the fiber-optic cable, the reflecting light spectrum is modulated in the sensor, depending on the cavity length and, therefore, on the applied pressure. Each wavelength λ of incoming light, which occurs to be an integer multiple N and fulfills the Fabry-Pérot resonance condition in equation 4, will interfere destructively in reflection [3].

$$N\lambda = 2\mathrm{n}(L + \Delta L) = \frac{\phi}{2\pi} \qquad (4)$$

An increasing cavity length $L + \Delta L$ shifts the phase condition of the destructively interfered wavelength in the spectrum to larger wavelengths, while smaller cavity length shifts the optical spectrum to shorter wavelengths. The variable n describes the refractive index of the air or vacuum inside the cavity, which is kept stable. The reflection spectrum R of the sensor is calculated by equation 5, which includes the mirror reflection coefficients $R1$, $R2$, the round-trip propagation phase shift ϕ of the interferometer [3].

$$R = \frac{R1+R2+2\sqrt{\mathrm{R1R2}}\cos(\phi)}{1+R1R2+2\sqrt{\mathrm{R1R2}}\cos(\phi)} \qquad (5)$$

The end face of the single-mode fiber and the polished glass membrane function as mirrors. This setup is known as an extrinsic fiber Fabry Perot interferometer in the literature.

2.2. Manufacturing of the Fabry-Pérot sensing head

Figure 2 illustrates the internal design of the sensing head. A fused silica Micro-Opto-Electro-Mechanical-Systems (MOEMS) is micromachined by a selective laser etching process.

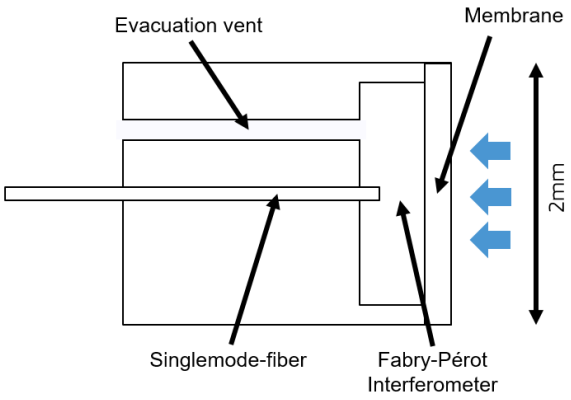

Figure 2. Sectional plane of the sensor head. The applied pressure bends the membrane and is influencing the resonator length.

The three-dimensional structure is inscribed in a quartz glass wafer by pulsed laser radiation in a first step. The light exposure is changing the glass properties locally in the focal volume. In consequence, a wet-chemical etching solvent reacts to processed areas with higher selectivity. [6] Due to the fundamental optical properties of the sensor, a second polished wafer is laser-welded on the carrier structure, and a light diffuser on the outside is added. In the next step, the sensor shape is etched or cut. For further manufacturing of the sensor, a single-Mode fiber is cleaved and bonded to the sensing head so that the destructive phase condition matches the operating point of the interrogator. Depending on the application, the sensor can be used as a differential sensor, sealed, or be hermetically packaged in a vacuum chamber to ensure static measurement by closing the second inlet by low outgassing adhesives. To minimize temperature cross-sensitivity, the sensor is shaped in fused silica, featuring a very low coefficient of thermal expansion. Additionally, by reducing the tolerances of the fiber inlet to its minimum, the most influence of the epoxy, which required to bond the fiber, is decreased.

2.3. Optical Interrogator for Static and Dynamic Measurement

In the optical fiber measurement industry, different approaches for the design of an interrogator to read out the Fabry-Pérot interferometer exist. A passive edge filter interrogator is not suitable for multiplexing Fabry-Pérot sensors but is a low-cost, reliable system and proven in the wind industry.

For this application, in combination with the introduced sensor, it is capable of measuring aerostatic, aerodynamic, and acoustic events up to 50 kHz sampling frequency. The acoustic noise floor of this measurement system is down to 60dBSPL. After illuminating the sensor with a broadband light source, the reflected light from the Fabry-Pérot interferometer splits into two parts in the measurement device. While the first part focuses directly on a photodiode, the second part is wavelength-dependent filtered and linked afterward on a second photodiode. The ratio P of the light intensities reveals the phase shift the reflected spectrum, which varies with the applied pressure and is compensating cross-sensitivities due to fiber bending, transmission loss, and fluctuations of the optical light power. The linear relationship between the shift of the Fabry-Pérot sensor and filtered intensity is inversely proportional to the detection resolution. The internal wavelength-dependent filter determines the spectral characteristics of the sensor, which needs to have a broader free spectral range than the spectral bandwidth of the internal filter.

2.4. Calibration

To calibrate the measurement setup for dynamic applications, the most straightforward approach is to use a pistophone, which outputs a sine pressure at specific amplitude and frequency. By recording this sound level and due to the constant transfer function of the sensor, the procedure obtains calibration factor k. The measured ratio of the photodiodes, substracted by its mean and multiplied with this multiplication factor, equals the applied dynamic pressure. Figure 3 illustrates the power spectral density of the dynamic calibration at 1 kHz with 114 dBSPL. The noise floor is constant over the bandwidth and equals down to almost 0.001Pa^2/Hz.

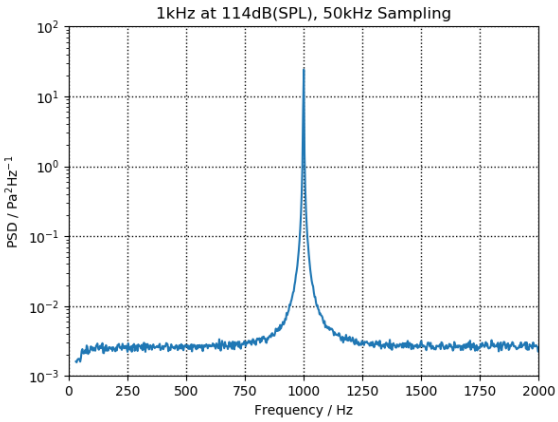

Figure 3. The power spectral density of a cylindrical sensor demonstrates that it can be used as a microphone as well due to the low noise.

Another obvious way is to use a static calibration tool for static pressure changes on the sensor. In this case, the pressure calibrator traverses the entire measurement characteristics. Figure 4 shows a relationship between the measured ratio and the applied pressure for a sensor and interrogator. Although the relation between the optical phase shift and the applied force is linear, the wavelength-dependent filter of the interrogator is trimming it to an S-line shape in the calibration curve. The measurement setup is used in the linear region, which is limiting the measurement range but avoids signal distortion in amplitude, frequency, or phase.

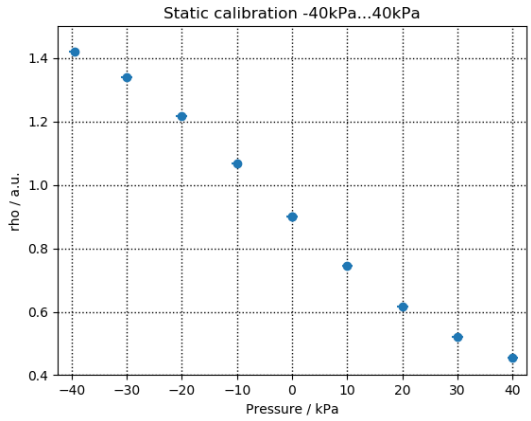

Figure 4. Calibration curve of a fiber-optic pressure sensor. The calibrated sensor around ambient pressure.

3. EXPERIMENTAL VALIDATION

Besides testing in the laboratory, two wind tunnel tests were carried out as part of the Cleansky2 project SKOPA (Skin friction and fiber-optics-based surface pressure measurements for aircraft applications). The project's goal is to design and fabricate a complete, flight-ready measurement system based on hot-film sensors for skin-friction measurements and fiber-optic sensors for time-resolved surface pressure measurement. The measurement technologies are validated in the lab, and in-flight tests are performed to prove airworthiness. As part of the Cleansky 2 project, the results obtained are additionally supposed to demonstrate and quantify the effect of active flow control (AFC) oscillators on aerodynamic structures close to stall conditions. Concerning lift gain and drag reduction, previous research projects have proven that a highly loaded compressor stator cascade leads to an increase in efficiency of 5% [7]. In addition to all validation measurements in the wind tunnel, this project concentrates on the beneficial effect of pulsed fluid jets for active flow control.

3.1. Low-speed wind-tunnel tests

The first low-speed wind tunnel tests have been performed to investigate the dynamic characteristics of the fiber-optic measurement setup. Therefore, the leading edge of this test setup has been equipped with a fluidic actuator system that is capable of forcing active oscillating air streams inside the boundary layer. During this wind channel test, eight differential pressure sensors were under test conditions. Figure 5 illustrates the setup.

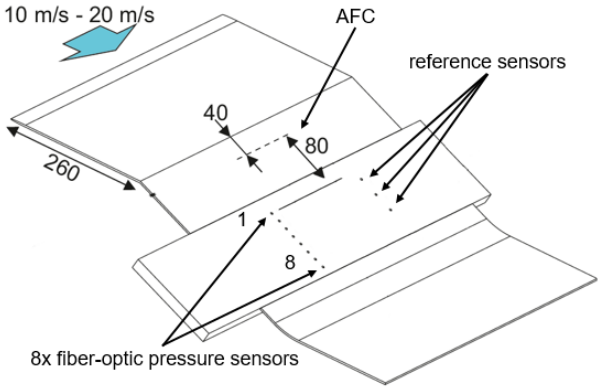

Figure 5. Test Setup of the first low-speed wind tunnel test. Inflow coming from left to right is influenced by active flow control oscillator (AFC).

Figures 6 and 7 demonstrate the system is capable of resolving high-frequency fluctuations in the pressure field propagation. By bandpass filtering and correlating the time-series signal, the propagation speed and direction are traced. In this setup, the sensors are aligned in a row and the steady inflow is not tilted to the sensor chained in a row. The sensor signals in the figure are normalized and shifted to make comprehension easier. The time-series 10..60Hz and 700…725Hz illustrate the propagation direction of the pressure fields at a 10m/s flow rate. The most bottom sensor signal, which is representing the first sensor inline, encounters the inflow firstly.

The time signals of the sensors in figure 8 illustrate static pressure measurements. At the start of the measure, due to the edge in front of the AFC, an unevenly static pressure field is caused. As soon as the AFC is switched on, the pressure fields alter and the static pressure levels on all sensor positions, especially positions 3 and 6, change.

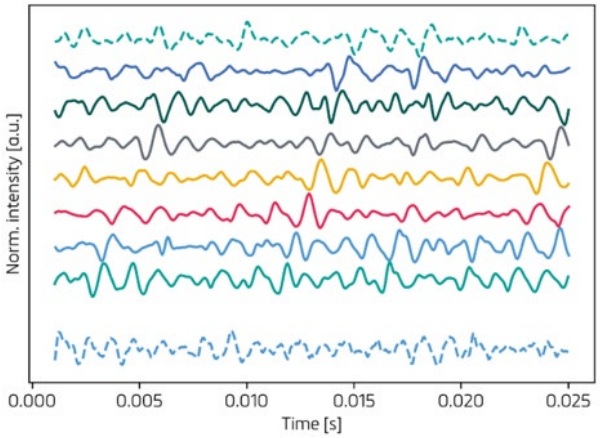

Figure 6. The normalized and bandpass filtered time-series from 10 to 60 Hz of differential pressure sensors at 10m/s flow rate show the propagation pressure fields. The most bottom signal is measured by the first sensor encountered by inflow.

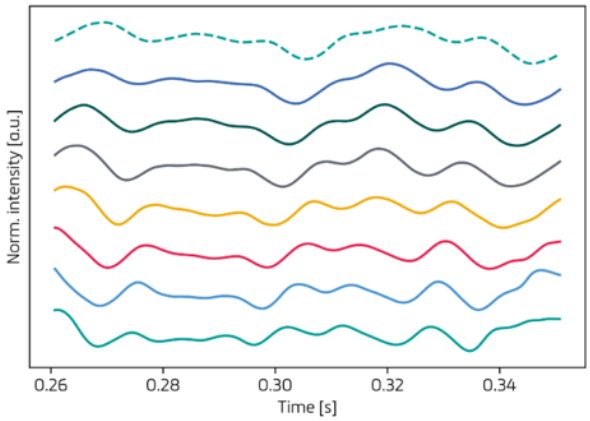

Figure 7. The normalized and bandpass filtered time-series from 700 to 725Hz of differential pressure sensors. The most bottom signal is the measurement by a reference sensor close to the AFC. The sensor signal in the first line was recorded by the sensor located with the largest distance to the AFC.

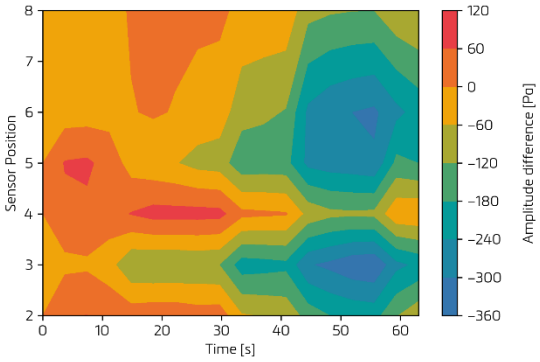

Figure 8. Static signal measurements (1Hz signals) indicate stationary pressure fields as soon as AFC triggers its airflow at around 30 s.

3.2. High-speed wind-tunnel tests

In the latest high-speed wind tunnel test, the static and dynamic performance of nine fiber-optic pressure sensors were evaluated up to M=0,5. To generate a complex three-dimensional flow, a bump and an AFC is integrated into this test setup to trigger flow separation. Figure 9 illustrates the measurement setup including the bump and AFC.

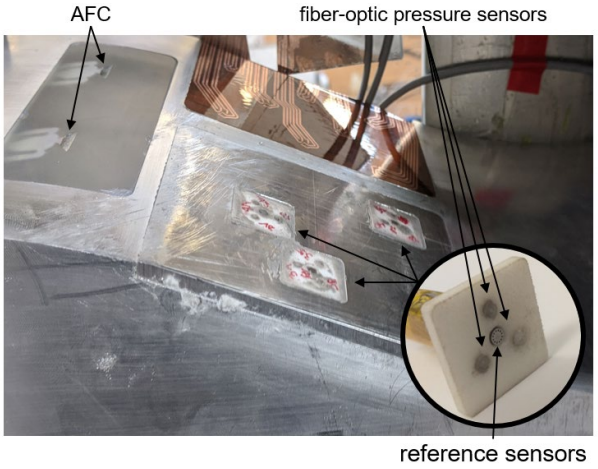

Figure 9. Setup of the second high-speed wind-tunnel test. Inflow coming from left to right is influenced by AFC to generate a complex airflow.

In order to benchmark fiber-optic sensors, 3x additional reference sensors were closely located to groups of 3x fiber-optic sensors. The reference sensors used were sampled a 1 kHz, while the fiber-optic sensor measured up to 10 kHz. Figure 10 shows an example of the pressure reading of a fiber-optic sensor in comparison with a Kulite reference sensor used as a reference. With increasing Mach number from 0.2 up to 0.5, more suction is generated. Additionally, the AFC has been switched on and off at each wind speed iteration, which is influencing the static lift as well and is triggering dynamic inflow.

The fiber-optic sensors match the reference sensors very well. While sensors located at the leading edge measured suction, sensors located at a larger distance measured static down thrust due to the high angle of attack and detached airflow.

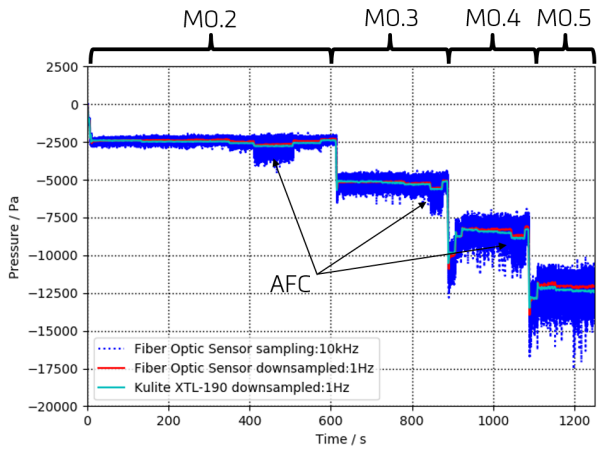

Figure 10. The time-series of the pressure signal shows a great match. With increasing Mach number from 0.2 up to 0.5, more suction has been generated. Additionally, the AFC has been switched on and off at each wind speed iteration, which is influencing the static lift as well.

Moreover, the dynamic performance of the pressure sensors was evaluated. The power spectral density of the sensors demonstrates its capabilities as a dynamic sensor or a microphone. The typical influence of the AFC is shown in figure 11. If the AFC is switched on, the oscillating mechanism generates a high-frequent noise as sound, which is depending on the volume flow. Additionally, we can observe that the active AFC is creating more dynamic streams at low frequencies and additionally is improving the static lift for this sensor. In figure 11, the measurement results of the fiber-optic setup are compared to the reading of reference sensor XT-140M. The electrical measurement setup displays the same results for the low frequency region but is not capable of measuring dynamics because of the low cut off frequency of the interrogator.

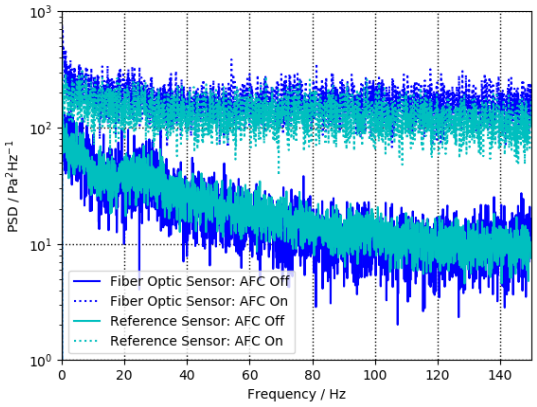

Figure 11 Typical PSD of measurement demonstrating the effect of the AFC in the low dynamic region. Comparing the Kulite XT-140M as a reference with fiber-optic sensor reading show a great match.

Nevertheless, the fiber-optic measurement system, sampling, and having a cut-off frequency at 10 kHz measures all dynamic turbulences and the sound noise generated by the AFC, as in figure 12.

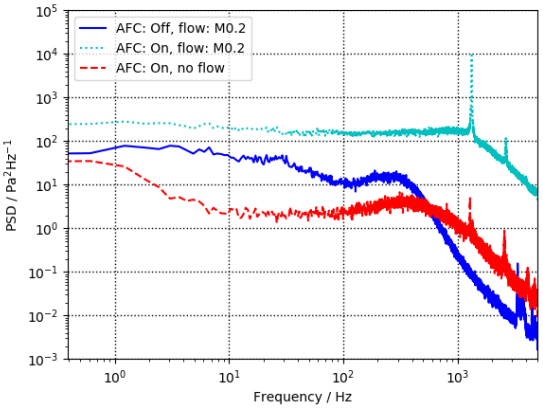

Figure 12 Typical PSD of measurement of the bump. If the AFC is switched on, dynamic turbulences interfere with the laminar airflow. Moreover, the AFC generates the typical switching frequency as a noise source.

Compared to figure 12, figure 13 illustrates the PSD of a sensor at the end of the bump section. This sensor measures the same flow conditions if the AFC is switched off. Nonetheless, if the AFC is interfering flow and changing the low frequent dynamics. Because of the larger distance to the AFC, the noise seems to be more isolated. Additionally, the frequency from 100 Hz to 1 kHz is more damped than for the sensor closer to the AFC.

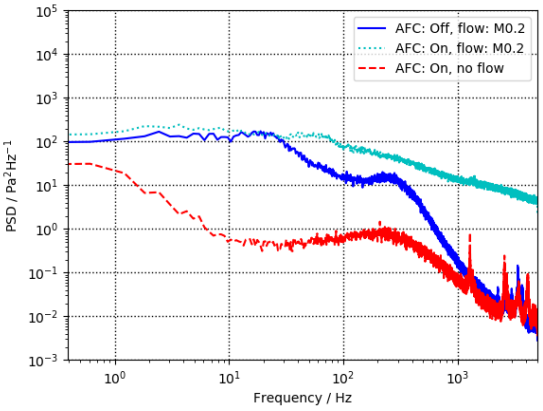

Figure 13. Spectrogram of a sensor at the trailing edge of a bump with the largest distance to the AFC. The AFC affects the turbulent flow as well. But the switching frequency of the AFC is not detected in flow conditions.

Figure 14 illustrates this relationship in a spectrogram. On this occasion, the wind tunnel settled at M0.2, and the volume flow of the AFC was increased up to 213 l^3/min. The illustration demonstrates the effect of the AFC for this sensor position very well. By increasing the volume flow, the triggered dynamic vortex flows influence the static suction on this sensor position, which is represented by the down sampled sensor signal.

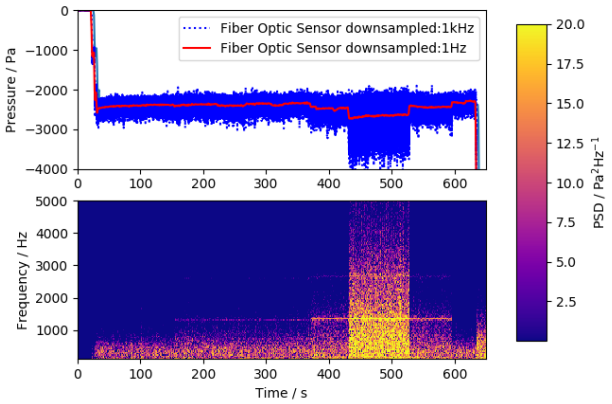

Figure 14. Spectrogram of a sensor. AFC generates a specific frequency pattern, regardless of volume flow. Additionally, the AFC affects the static lift by reattachment of laminar flow.

4. DISCUSSION AND OUTLOOK

We have developed a cylindrical shaped fiber-optic pressure sensor. Due to the fiber-optic design, those sensors are well suitable for harsh testing in-flight tests. For validation, in two wind tunnel campaigns, seventeen sensors have been mounted in a low-speed and high-speed wind tunnel, which were equipped with active flow control. The sensors have been compared to their electrical counterparts.

The results demonstrated the competitive performance. These first tests pave the way for performing in-flight measurements of time-resolved surface pressure near the wing-pylon interface of a transport aircraft. To prove the flight capabilities of the measurement setup, the following objective will be the evaluation of measurements on a light sports aircraft in relevant conditions at the beginning of 2020.

5. ACKNOWLEDGMENTS

The authors thank the European Union for the funding of the project “Clean Sky 2 – SKOPA JTI-CS2-2017-CFP07-LPA-01-39 (Skin friction and fiber-optics-based surface pressure measurements for aircraft applications)”. Additionally, the authors thank all project partners within the project.

6. REFERENCES

1. M.J. Gander, W.N. MacPherson, J.S. Barton, R.L. Reuben, J.D.C. Jones, R. Stevens, K.S. Chana, S.J. Anderson & T.V. Jones, (2003) “Embedded Micromachined Fiber-Optic Fabry–Pérot Pressure Sensors in Aerodynamics Applications” IEEE Sensors Journal (Volume: 3, Issue: 1 , Feb. 2003)

2. P. Schloesser, V. Soudakov, M. Bauer & J. Wild, (2018) “Active Separation Control at the Pylon-Wing Junction of a Real-Scale Model” AIAA JOURNAL (Volume: 57, Number: 1 , Jan. 2019)

3. S. Yin, P.B. Ruffin & F. Yu, Fiber-optical Sensors (2018), 2nd edn, Optical Science and Engineering Series. Boca Raton FL: CRC Press

4. G.C. Hill, R. Melamud, F.E. Declercq, A.A. Davenport, I.H. Chan, P.G. Hartwell & B.L. Pruitt (2007), “SU-8 MEMS Fabry-Perot pressure sensor”, Sensors and Actuators A 138, 52–62

5. M.J. Schmid, B.A. Kuhnle, S.U. Kienitz, A. Altmikus, C.F. Napierala, C. Scheit, M.S. Müller & A.W. Koch (2017) “A fiber-optic sensor for measuring quasi-static and unsteady pressure on wind energy converters” Smarte Strukturen und Systeme, Tagungsband des 4SMARTS-Symposiums

6. J. Gottmann, M. Hermans, N. Repiev & J. Ortmann (2017) “Selctive Laser-Induced Etching of 3D Precision Quartz Glass Componets for Microfluid Applications – Up-Scaling of Complexity and Speed”, Micromachines 2017, 8, 110

7. M. Staats, S. Löffler, C. Ebert, T. Grund & J. Weiss (2018) “A Fluidic Device for Active Flow Control: Simulation vs. Experiment with Emphasis on Application”, AIAA AVIATION Forum 2018 Applied Aerodynamics Conference